

Cite this: *Chem. Sci.*, 2025, 16, 6035

All publication charges for this article have been paid for by the Royal Society of Chemistry

## Reversible enzyme-catalysed $\text{NAD}^+/\text{NADH}$ electrochemistry†

Peter D. Giang,<sup>a</sup> Dimitri Niks,<sup>b</sup> Sheron Hakopian,<sup>b</sup> Russ Hille<sup>b</sup> and Paul V. Bernhardt<sup>\*a</sup>

Formate dehydrogenase (FdsDABG) from *Cupriavidus necator* is a Mo-containing enzyme capable of catalysing both formate oxidation to  $\text{CO}_2$  and the reverse  $\text{CO}_2$  reduction to formate by utilising  $\text{NAD}^+$  or NADH, respectively. This enzyme is part of the NADH dehydrogenase superfamily. Its subcomplex, FdsBG, lacking the formate oxidizing/ $\text{CO}_2$ -reducing Mo-cofactor, but harbouring an FMN as well as [2Fe–2S] and [4Fe–4S] clusters, reversibly interconverts the  $\text{NAD}^+/\text{NADH}$  redox pair. UV-vis spectroelectrochemistry across the range  $6 < \text{pH} < 8$  determined the redox potentials of these three cofactors. Cyclic voltammetry was used to explore mechanistic and kinetic properties of each oxidation- and reduction-half reaction. Through mediated enzyme electrochemistry experiments, the Michaelis constant for NADH oxidation ( $K_{\text{M,NADH}} = 1.7 \times 10^2 \mu\text{M}$ ) was determined using methylene blue as a redox mediator. For the reverse  $\text{NAD}^+$  reduction reaction using methyl viologen as electron donor a similar analysis yielded the value of  $K_{\text{M,NAD}^+} = 1.2 \text{ mM}$ . All experimental voltammetry data were reproduced by electrochemical simulations furnishing a set of self-consistent rate constants for the catalytic FdsBG system for both  $\text{NAD}^+$  reduction and NADH oxidation. This comprises the first electrochemical kinetic analysis of its kind for a reversible NADH dehydrogenase enzyme and provides new insight to the function of the FdsDABG formate dehydrogenase holoenzyme.

Received 22nd January 2025  
Accepted 3rd March 2025

DOI: 10.1039/d5sc00570a

rsc.li/chemical-science

## Introduction

Reduced nicotinamide adenine dinucleotide (NADH) and its phosphate analogue NADPH are ubiquitous and essential reductants involved in numerous biochemical pathways principally as hydride donors. Given the widespread use of NAD(P)H as a reductant of many enzymes and its commercial cost, there is interest in its regeneration,<sup>1</sup> but the selective non-biological reduction of  $\text{NAD(P)}^+$  to NAD(P)H (1,4-dihydro isomer) is difficult. Non-biologically active byproducts (1,2- and 1,6-dihydro isomers and NADH dimers) are a particular issue.<sup>2,3</sup> In contrast to synthetic methods,<sup>4</sup> many oxidoreductase enzymes are capable of regenerating NAD(P)H from  $\text{NAD(P)}^+$  with high specificity and efficiency, including glucose dehydrogenase,<sup>5</sup> hydrogenase,<sup>6</sup> alcohol dehydrogenase,<sup>7,8</sup> phosphite dehydrogenase<sup>9,10</sup> and formate dehydrogenase.<sup>11–13</sup> Despite multiple enzyme candidates for this reaction, typical biochemical problems exist for some of these enzymes that limit scale-up. Utilisation of these enzymes for NAD(P)H regeneration to support

other enzyme systems introduces complexity, with multiple active enzymes and co-substrates present.<sup>14</sup> Further drawbacks include the difficulty in selectively separating out NAD(P)H from a complex enzymatic mixture which may still include structurally similar  $\text{NAD(P)}^+$ .<sup>15</sup> Furthermore, the aforementioned enzyme candidates have displayed limited pH-, temperature-, and air-stability.<sup>16–18</sup>

One enzyme of particular interest is the Mo-containing formate dehydrogenase (FdsDABG) from the Gram-negative soil bacterium *Cupriavidus necator* (*C. necator*), which is air-stable, can reversibly catalyse both formate oxidation to  $\text{CO}_2$  and  $\text{CO}_2$  reduction to formate, and is also a member of the NADH dehydrogenase family.<sup>19</sup> Given its stability and catalytic ability, FdsDABG has been explored in biotechnological applications.<sup>20–22</sup> Cryo-EM studies of FdsDABG from *Rhodobacter capsulatus* (*R. capsulatus*), which shares high sequence homology with FdsDABG from *C. necator*, revealed the spatial disposition of these cofactors within the heterotetrameric protomer which is illustrated in cartoon form in Fig. 1.<sup>23</sup> The FdsA subunit (105 kDa) contains the molybdenum centre (the site of formate oxidation and  $\text{CO}_2$  reduction), one [2Fe–2S] cluster and four [4Fe–4S] clusters. The FdsB subunit (55 kDa) contains one [4Fe–4S] cluster and a flavin mononucleotide (FMN), which is the NADH/ $\text{NAD}^+$  binding site. The FdsG subunit (19 kDa) contains a single [2Fe–2S] cluster.<sup>24</sup> The small (7 kDa) FdsD subunit (not shown in Fig. 1) has no redox-active cofactors but is

<sup>a</sup>School of Chemistry and Molecular Biosciences, University of Queensland, Brisbane 4072, Australia. E-mail: p.bernhardt@uq.edu.au

<sup>b</sup>Department of Biochemistry, University of California, Riverside, USA

† Electronic supplementary information (ESI) available: Comprising structures of all redox mediators, optical spectroelectrochemistry data, cyclic voltammetry control experiments without enzyme and all electrochemical simulation parameters. See DOI: <https://doi.org/10.1039/d5sc00570a>

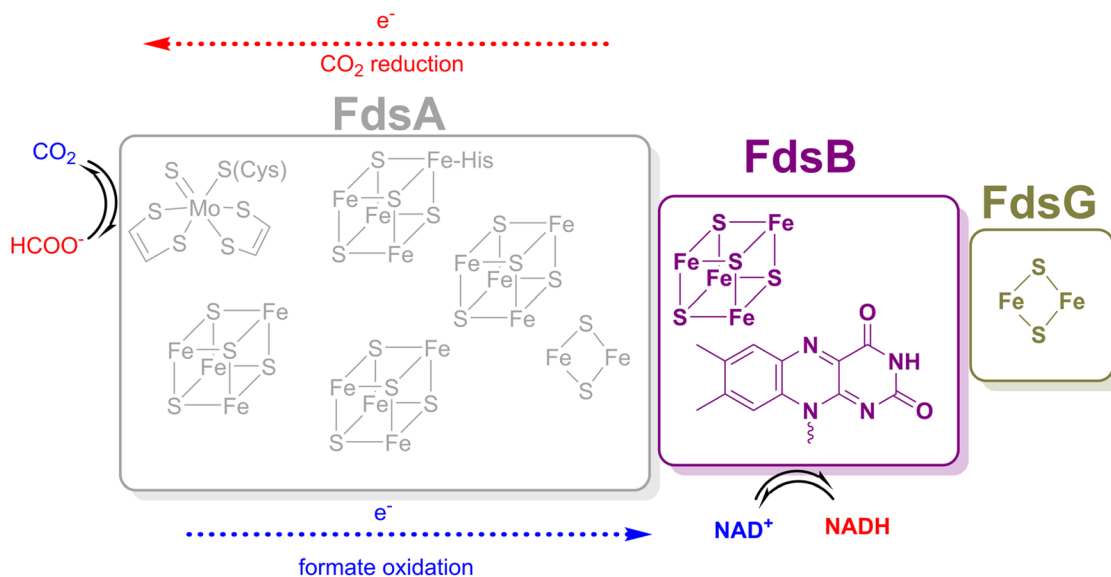


Fig. 1 Cartoon representation of the FdsA, FdsB, and FdsG subunits and their respective cofactors of FdsDABG from *C. necator*. The FdsD subunit is not shown as it does not contain any cofactors.

thought to be involved in Mo cofactor maturation and insertion.<sup>25</sup>

The combination of structural complexity and relative oxygen tolerance of FdsDABG has prompted investigations into its mechanism and function.<sup>26</sup> Recent redox characterisation of the cofactors in *C. necator* FdsDABG was achieved through a combination of EPR-monitored redox potentiometry and optical spectroelectrochemistry on both the holoenzyme FdsDABG and its subcomplex FdsBG.<sup>27</sup> The FdsBG subcomplex has also been crystallographically characterised.<sup>24</sup> A partial redox characterisation of the homologous FdsDABG from *R. capsulatus* has subsequently been reported.<sup>28</sup>

The focus of this study is electrochemical activation of the FdsBG subcomplex as a reversible  $\text{NAD}^+/\text{NADH}$  oxidoreductase. Isolated FdsBG exhibits  $\text{NADH}:\text{O}_2$  oxidoreductase (diaphorase) activity,<sup>24</sup> although within the FdsDABG holoenzyme the native function of the (reduced) FMN cofactor is to reduce  $\text{NAD}^+$  rather than oxidise NADH. The system thus presents an ideal example of a bidirectional  $\text{NADH}/\text{NAD}^+$  redox system. To date, investigations into  $\text{NAD}^+$  reduction and NADH oxidation have only been performed through steady-state and stopped flow single-turnover kinetic experiments.<sup>19,22,24,26</sup> The electrochemical approach taken here removes the need for chemical reductants (dithionite) which may obscure important spectroscopic information. We have also explored the use of both single- and two-electron redox mediators and have undertaken a full kinetic analysis using electrochemical simulations. This study represents a new approach to expensive nicotinamide recycling, which remains an area of considerable biotechnological importance.<sup>29,30</sup> The mechanistic information emerging from this analysis reveals previously inaccessible kinetic data that not only explains the high  $\text{NADH}/\text{NAD}^+$  recycling activity of the FdsBG subcomplex but also the FdsDABG holoenzyme.

## Experimental

### Protein purification

The FdsBG subcomplex was expressed, purified, and characterised according to a published procedure<sup>24</sup> and was stored frozen ( $-80^\circ\text{C}$ ) in phosphate buffer (50 mM, pH 7.5) at a concentration of 178  $\mu\text{M}$ .

### Reagents

The organic mediators phenazinium (PMS, methosulfate salt), methylene blue ( $\text{MB}^+$ , chloride salt), methyl viologen ( $\text{MV}^{2+}$ , chloride salt) and Safranin T (chloride salt) were all obtained commercially. Transition metal mediators for spectroelectrochemistry included  $[\text{Fe}(\text{trans-diammac})](\text{ClO}_4)_3$ ,<sup>31</sup>  $[\text{Co}(\text{AMMEN}_4\text{S}_2\text{sar})]\text{Cl}_3$ ,<sup>32</sup>  $[\text{Co}(\text{AMMEN}_5\text{Ssar})]\text{Cl}_3$ ,<sup>33</sup>  $[\text{Co}(\text{sep})]\text{Cl}_3$ ,<sup>34</sup>  $[\text{Co}(\text{AMMESar})]\text{Cl}_3$ ,<sup>35</sup>  $[\text{Co}(\text{ClMeClAbsar})]\text{Cl}_3$ ,<sup>35</sup> and  $[\text{Co}(\text{cis-diammac})](\text{ClO}_4)_3$ .<sup>36</sup> The structures of all mediators are given in the ESI (Fig. S1).† All other reagents were obtained commercially at analytical grade and were used as purchased. All solutions were prepared using ultrapure water (18.2  $\text{M}\Omega\text{ cm}$ ).

### UV-vis spectroelectrochemistry

Optical (UV-vis) spectroelectrochemical experiments were performed in a quartz spectroelectrochemical cell (1.7 mm path length) with a gold “honeycomb” working electrode (Pine Instruments), a gold auxiliary electrode and a  $\text{Ag}/\text{AgCl}$  reference electrode calibrated with quinhydrone at pH 7 ( $E_{\text{m},7} + 0.285\text{ V vs. NHE}$ ). The cell contained an approximately 600  $\mu\text{L}$  solution comprising FdsBG (approximately 100  $\mu\text{M}$ ), and redox mediators. These included  $[\text{Fe}(\text{trans-diammac})]^{3+}$ ,  $[\text{Co}(\text{AMMEN}_4\text{S}_2\text{sar})]^{3+}$ ,  $[\text{Co}(\text{AMMEN}_5\text{Ssar})]^{3+}$ ,  $[\text{Co}(\text{sep})]^{3+}$ ,  $[\text{Co}(\text{AMMESar})]^{3+}$ ,  $[\text{Co}(\text{ClMeClAbsar})]^{3+}$ , and  $[\text{Co}(\text{cis-diammac})]^{3+}$  (each 80  $\mu\text{M}$ ). The  $\text{M}^{\text{III/II}}$  ( $\text{M} = \text{Fe}, \text{Co}$ ) redox couples of these complexes are reversible and their potentials span the oxidation-reduction potential (ORP)



range 0 to  $-0.55$  V vs. NHE (Fig. S1†). They also exhibit low molar absorption coefficients in the visible region ( $\epsilon < 500 \text{ M}^{-1} \text{ cm}^{-1}$ ) resulting in negligible spectral interference at the micromolar concentrations used.<sup>37,38</sup> UV-vis spectra were acquired with an Agilent 8453 diode array UV-vis spectrophotometer, with the cell cooled to  $15^\circ \text{C}$  by a Huber Ministat 230 refrigerated water-circulating bath. Applied potentials were controlled by a Gamry Interface 1010 potentiostat. UV-vis spectra were recorded at  $12.5$  mV intervals when electrochemical equilibrium was established and no further spectral changes were occurring. Reversibility was established upon returning from either more negative to more positive (or from more positive to more negative) potential with minimal spectral hysteresis. For single electron redox reactions, the relationship between spectral absorbance and applied potential ( $E$ ) is given by a combination of the Nernst equation and Beer-Lambert law as seen in eqn (1). In this equation,  $A_{\text{ox}}$  and  $A_{\text{red}}$  are the absorbances at that wavelength of the oxidised and reduced forms of the chromophore, and  $E_{\text{m}}$  is the midpoint potential (V).

$$\text{Absorbance} = \frac{\left( A_{\text{ox}} 10^{\frac{(E-E_{\text{m}})}{0.059}} + A_{\text{red}} \right)}{1 + 10^{\frac{(E-E_{\text{m}})}{0.059}}} \quad (1)$$

For two electron redox reactions, eqn (2) applies where  $E_1$  and  $E_2$  are the potentials of the first and second reductions.  $A_{\text{ox}}$ ,  $A_{\text{int}}$ , and  $A_{\text{red}}$  are the absorbances at a given wavelength of the three redox states.

$$\text{Absorbance} = \frac{\left( A_{\text{ox}} 10^{\frac{(E-E_1)}{0.059}} + A_{\text{int}} + A_{\text{red}} 10^{\frac{(E_2-E)}{0.059}} \right)}{1 + 10^{\frac{(E-E_1)}{0.059}} + 10^{\frac{(E_2-E)}{0.059}}} \quad (2)$$

The potential-dependent spectra were modelled by global analysis with ReactLab Redox<sup>39</sup> that fits the potential dependent absorbance data (at all wavelengths) to eqn (1) and (2). These data are collected in Table 1. All experimental data are given in the ESI (Fig. S2)† with spectral analyses at pH 6 (Fig. S3†) and pH 8 (Fig. S4†).

## Electrochemical measurements

Cyclic voltammetry (CV) experiments were conducted at  $25^\circ \text{C}$  with a BASi EC Epsilon potentiostat using a three-

electrode system comprising a glassy carbon disk working electrode, platinum wire counter electrode, and Ag/AgCl reference electrode. The glassy carbon electrode was polished mechanically in a slurry of alumina ( $0.05 \mu\text{m}$ ) in ultrapure water on a microfibre polishing pad. The electrode was then sonicated in ultrapure water for 15 minutes to give a mirror-like finish.

The electroactive surface of the glassy carbon electrode was calculated from the cyclic voltammogram of  $1 \text{ mM}$  ferrocene methanol in  $0.1 \text{ M}$  KCl solution at multiple scan rates using the Randles-Sevcik equation (eqn (3)).<sup>40</sup> The diffusion coefficient ( $D$ ) of ferrocene methanol is  $6.7 \times 10^{-6} \text{ cm}^2 \text{ s}^{-1}$ ,<sup>41</sup>  $i_p$  is the CV current maximum,  $n$  is the number of electrons (here  $n = 1$ ),  $C$  is the concentration of analyte ( $\text{mol cm}^{-3}$ ), and  $v$  is the sweep rate ( $\text{V s}^{-1}$ ). The surface area was determined to be  $A = 0.056 \text{ cm}^2$ .

$$i_p = 2.69 \times 10^5 D^{1/2} n^{3/2} A C v^{1/2} \quad (3)$$

The diffusion coefficients of the methyl viologen dication/radical monocation ( $\text{MV}^{2+/+}$ ) and the methylene blue monocation/neutral leuco form ( $\text{MB}^+/\text{MBH}$ ) were also determined using eqn (3) and the above value of  $A$  in a similar fashion. Linear regression of  $i_p$  versus  $v^{1/2}$  gave values of  $D(\text{MV}^{2+/+}) = 3.8 \times 10^{-6} \text{ cm}^2 \text{ s}^{-1}$  and  $D(\text{MB}^+/\text{MBH}) = 2.1 \times 10^{-6} \text{ cm}^2 \text{ s}^{-1}$ , which are consistent with published work.<sup>42,43</sup>

## Catalytic voltammetry

The electrochemical solution ( $2.5 \text{ mL}$   $50 \text{ mM}$  phosphate, pH 7.5) contained methyl viologen ( $60 \mu\text{M}$ ) or methylene blue ( $20 \mu\text{M}$ ) and was purged with  $\text{N}_2$ . These concentrations were sufficiently high to obtain a good signal to noise ratio. Higher mediator concentrations gave relatively smaller changes as a function of substrate concentration in accord with theory.<sup>44</sup> FdsBG ( $0.34 \mu\text{M}$ ) was added to the solution and mixed by gentle stirring ( $50 \text{ rpm}$ ) under a blanket of  $\text{N}_2$ . Small aliquots of stock solutions of  $\text{NAD}^+$  or  $\text{NADH}$  were added and mixed to give bulk concentrations described in the text. Cyclic voltammograms were then run on quiescent solutions at scan rates from  $2$  to  $20 \text{ mV s}^{-1}$ . The catalytic currents ( $i_{\text{lim}}$ ) were taken as the nett current once the contribution from the mediator current (at zero substrate concentration) was subtracted (at  $-0.55 \text{ V}$  for  $\text{MV}^{2+}$  or  $+0.15 \text{ V}$  for  $\text{MB}^+$ ). The currents were modelled as a function of substrate ( $S$ ) concentration with the Michaelis-Menten equation (eqn (4)).

$$i_{\text{lim}} = \frac{i_{\text{max}}[S]}{K_M + [S]} \quad (4)$$

**Table 1** Redox potentials (V vs. NHE) of the [4Fe–4S], FMN and [2Fe–2S] cofactors present in FdsBG at different pH values as determined through optical spectroelectrochemistry. In this study, pH 6, 7 and 8 are new data. Data for pH 7.5 are from previous work<sup>27</sup>

	pH 6	pH 7	pH 7.5 (ref. 27)	pH 8
[4Fe–4S] <sup>2+/+</sup>	—	−0.45	−0.49	−0.48
FMN/FMNH <sup>•</sup>	−0.24	−0.25	−0.30	−0.32
FMNH <sup>•</sup> /FMNH <sup>−</sup>	−0.31	−0.34	−0.38	−0.37
[2Fe–2S] <sup>2+/+</sup> (deflavo form <sup>a</sup> )	−0.12 (−0.15)	−0.15 (−0.19)	−0.13 (−0.21)	−0.13 (−0.20)

<sup>a</sup> Tentative assignment of the more negative [2Fe–2S]<sup>2+/+</sup> redox potential to deflavo-FdsBG.



where  $i_{\max}$ , the limiting current at saturating concentration of substrate (proportional to the turnover number) and  $K_M$  is the Michaelis constant.<sup>45</sup> Under a given set of conditions (pH, enzyme and mediator concentrations)  $i_{\max}$  will be a constant.

### pH dependent measurements

Seven different buffer solutions (each 50 mM) were prepared, with pH values ranging from 6 to 9 in 0.5 pH unit increments adjusted with dilute NaOH or AcOH: citrate (pH 6), phosphate (pH 6.5, pH 7, and pH 7.5), bicine (pH 8 and pH 8.5), and CHES (2-(cyclohexylamino)ethane-1-sulfonic acid, pH 9). All pH measurements were made and rechecked *in situ* in the electrochemical cell with a Hanna 8424 pH meter and Hanna HI-1093B pH electrode (Microbulb).

For NAD<sup>+</sup> reduction experiments, to each of the above buffer solutions (2.5 mL) was added methyl viologen (12.5  $\mu$ L of 10 mM) to give a final concentration of 60  $\mu$ M. The solution was purged with N<sub>2</sub> for a few minutes, the gas inlet tube was withdrawn from the solution and a blanket of N<sub>2</sub> was maintained throughout the experiment. FdsBG was added (5  $\mu$ L of 178  $\mu$ M) to give a final concentration of 0.34  $\mu$ M (active enzyme) after gently mixing with a magnetic stirrer (50 rpm). Stirring was discontinued and a CV was measured at a scan rate of 5 mV s<sup>-1</sup> which was used as a baseline measurement (zero activity). Under a blanket of N<sub>2</sub>, NAD<sup>+</sup> (125  $\mu$ L of 100 mM) was added and mixed with a magnetic stirrer for 10 min under a blanket of N<sub>2</sub> to give a 5 mM solution. Stirring was discontinued and the CV was measured.

The above procedure was repeated for all buffer solutions at their pH value. The differences in cathodic current at -0.55 V vs.

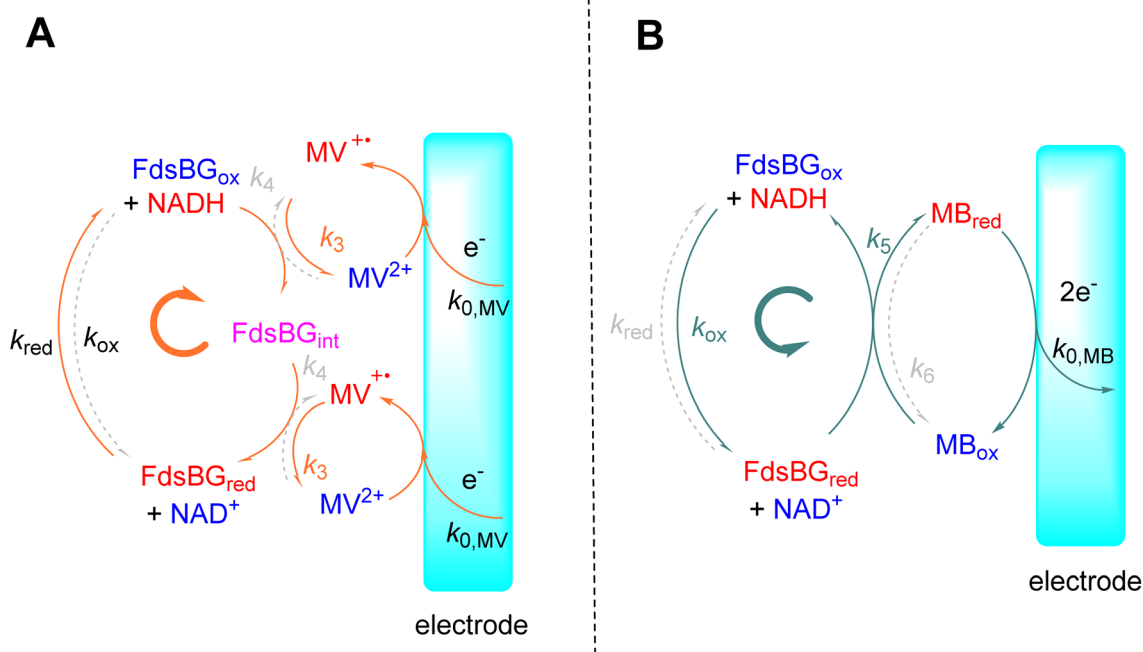
NHE with and without NAD<sup>+</sup> was taken as the value of  $i_{\max}$  and these data as a function of pH were fit to eqn (5) which is applicable for an enzyme that is deactivated by protonation of a base at acidic pH values ( $pK_{a2}$ ) or deprotonation of an acid at basic pH values ( $pK_{a1}$ ), and  $i_{\text{opt}}$  is the catalytic current at the optimal pH ( $(pK_{a1} + pK_{a2})/2$ ).

$$i_{\max}(\text{pH}) = \frac{i_{\text{opt}}}{1 + 10^{(\text{pH}-pK_{a1})} + 10^{(pK_{a2}-\text{pH})}} \quad (5)$$

For NADH oxidation experiments, methylene blue (5  $\mu$ L of 10 mM) was added to each of the above buffer solutions (2.5 mL) to give a final concentration of 20  $\mu$ M. As above, the solution was purged with N<sub>2</sub>, the gas supply tube was withdrawn from the solution whilst maintaining a blanket of N<sub>2</sub> then FdsBG was added (5  $\mu$ L of 178  $\mu$ M) to give a final concentration of 0.34  $\mu$ M (active enzyme). A CV was measured then NADH (125  $\mu$ L of 10 mM) was added with gentle stirring under a N<sub>2</sub> blanket to give a final concentration of 500  $\mu$ M. After 10 min stirring was discontinued and a CV was measured. This was repeated at each pH value and the current differences at +0.15 V vs. NHE with and without NADH were fit to eqn (5).

### Electrochemical simulation

The Digisim program (version 3.03b) was utilised to simulate the experimental cyclic voltammetry data.<sup>46</sup> The models for NAD<sup>+</sup> reduction/NADH oxidation are shown in Scheme 1. Cyclic voltammograms were acquired on solutions containing known concentrations of FdsBG, NAD<sup>+</sup>/NADH and mediator methyl viologen or methylene blue at scan rates in the range 2 to 20 mV



**Scheme 1** The model employed for electrochemical simulations of FdsBG-catalysed (A) NAD<sup>+</sup> reduction mediated by methyl viologen (orange solid arrows showing clockwise direction of cycle) and (B) NADH oxidation mediated by methylene blue (grey solid arrows – anticlockwise direction). The grey broken arrows show the reverse (unfavored) directions of each catalytic cycle.





$\text{s}^{-1}$ . The redox potentials of all mediators were determined from control experiments without FdsBG or substrate present. The diffusion coefficients of mediators  $\text{MV}^{2+/+}$  ( $3.8 \times 10^{-6} \text{ cm}^2 \text{ s}^{-1}$ ) and  $\text{MB}^+/\text{MBH}$  ( $2.1 \times 10^{-6} \text{ cm}^2 \text{ s}^{-1}$ ) were determined by CV herein as described above. A value of  $D(\text{NAD}^+/\text{NADH}) = 4.0 \times 10^{-6} \text{ cm}^2 \text{ s}^{-1}$  was taken from the literature.<sup>47</sup> The diffusion coefficient of FdsBG is unknown but its crystal structure<sup>24</sup> reveals a roughly spherical shape so based on its molecular weight ( $M = 74\,000 \text{ Da}$ ) a diffusion coefficient may be estimated<sup>48</sup> using eqn 6.

$$D = \frac{8.34 \times 10^{-8} T}{\eta M^{1/3}} \quad (6)$$

where  $T$  is the temperature (K) and  $\eta$  is the viscosity of the solvent (water  $1.00 \text{ cP}$ ). A value of  $D(\text{FdsBG}) = 5.9 \times 10^{-7} \text{ cm}^2 \text{ s}^{-1}$  was calculated (for all redox states). The heterogeneous rate constants for  $\text{MV}^{2+/+}$  and  $\text{MB}^+/\text{MBH}$  were obtained by simulation of the CV data in the absence of substrate and values of  $k_0 = 1 \times 10^{-2} \text{ cm s}^{-1}$  were obtained. The most important kinetic parameters are given in Table 2 while all simulation parameters are assembled in the ESI (Table S1).<sup>†</sup> The same set of rate constants reproduced 16 voltammograms measured at different scan rates and substrate concentrations (Fig. 7 and 8) so the rate constants represent a consensus set of values with uncertainties estimated to be 20% as reported previously.<sup>49</sup>

Given the symmetry of the  $\text{NAD}^+$  reduction/ $\text{NADH}$  oxidation reaction (Scheme 1A and B), the main mechanistic differences between FdsBG-catalysed  $\text{NAD}^+$  reduction and  $\text{NADH}$  oxidation are that  $\text{NAD}^+$  reduction comprises two consecutive one-electron reductions by  $\text{MV}^{2+}$  via an intermediate oxidation state ( $\text{FdsBG}_{\text{int}}$ ) while the 2-electron,  $\text{MB}$ -mediated  $\text{NADH}$  oxidation bypasses the intermediate FdsBG oxidation state. We have assumed the rates of the consecutive single electron transfer steps ( $k_3/k_4$ ) are equal as their driving forces are essentially the same and the site of binding will be the same regardless of whether  $\text{FdsBG}_{\text{ox}}$  or  $\text{FdsBG}_{\text{int}}$  is reacting. The two FMN redox potentials ( $\text{FMN}/\text{FMNH}^+$  and  $\text{FMNH}^+/\text{FMNH}^-$ ) lie between those of the  $[2\text{Fe}-2\text{S}]^{2+/+}$  and  $[4\text{Fe}-4\text{S}]^{2+/+}$  couples (Table 1) and  $\text{NAD}^+$  reduction/ $\text{NADH}$  oxidation must occur at the fully reduced/oxidised FMN active site, respectively. The model does not consider redox reactions at the  $[2\text{Fe}-2\text{S}]^{2+/+}$  and

$[4\text{Fe}-4\text{S}]^{2+/+}$  cofactors (intermolecular or intramolecular) which are unproductive in terms of substrate turnover at the FMN cofactor.

## Results and discussion

### Structural aspects

The cofactor positions within FdsBG have been established by X-ray crystallography<sup>24</sup> and this is shown in Fig. 2. Within the FdsB subunit, the  $[4\text{Fe}-4\text{S}]$  and FMN cofactors are in proximity ( $\sim 3.9 \text{ \AA}$ ) and trace the final two steps in electron transfer from the molybdenum centre (in the FdsA subunit of the FdsDABG holoenzyme) to  $\text{NAD}^+$  following formate oxidation (see Fig. 1). The FdsB  $[4\text{Fe}-4\text{S}]$  cluster lies close to the  $[2\text{Fe}-2\text{S}]$  cluster of FdsA in the holoenzyme (Fig. 1) and is 'on-path' for electron transfer from the molybdenum centre to FMN. The  $[2\text{Fe}-2\text{S}]$  cluster (in the FdsG subunit) is 'off-path' but still within electron transfer range ( $\sim 10.1 \text{ \AA}$ ) of the FMN. The amino acid residues Asp184 and Glu185 (in the FdsG subunit) are situated between the FMN and  $[2\text{Fe}-2\text{S}]$  cluster. The FMN cofactor is where  $\text{NAD}^+/\text{NADH}$  binds, and this has also been demonstrated crystallographically.<sup>24</sup>

### pH-dependent UV-vis spectroelectrochemistry

The three redox-active cofactors in Fig. 2 comprise a two-electron  $\text{FMN}/\text{FMNH}^+/\text{FMNH}^-$  couple and one-electron  $[4\text{Fe}-4\text{S}]^{2+/+}$  and  $[2\text{Fe}-2\text{S}]^{2+/+}$  couples. Each cofactor in its oxidised form influences the absorbance spectrum of FdsBG and they undergo typical UV-vis spectral changes upon reduction and oxidation. In their fully reduced forms the  $\text{FMNH}^-$ ,  $[4\text{Fe}-4\text{S}]^+$  and  $[2\text{Fe}-2\text{S}]^+$  cofactors become largely bleached throughout the UV-visible region. The redox potentials of FdsBG at pH 7.5 are known<sup>27</sup> but here we have extended this investigation over the pH range 6 to 8 to support pH-dependent electrochemical studies (presented in the next section).

The cofactor with most negative redox potential in FdsBG is the  $[4\text{Fe}-4\text{S}]^{2+/+}$  cluster, which has been characterised previously by UV-vis<sup>27</sup> and EPR<sup>24</sup> spectroscopy, while the  $[2\text{Fe}-2\text{S}]^{2+/+}$  cluster has the most positive potential. The closely spaced  $\text{FMN}/\text{FMNH}^+$  and  $\text{FMNH}^+/\text{FMNH}^-$  redox potentials lie between those

**Table 2** Kinetic parameters derived from electrochemical simulation of FdsBG-catalysed  $\text{NAD}^+$  reduction and  $\text{NADH}$  oxidation (see Scheme 1). Values in italics uncertain due to the reactions favouring  $\text{MV}^{2+}$  oxidation/ $\text{MB}^+$  reduction ( $k_3 \gg k_4$  and  $k_5 \gg k_6$ ). Proton transfer reactions are omitted for clarity

Mediator independent		
$\text{FdsBG}_{\text{red}} + \text{NAD}^+ \rightleftharpoons \text{FdsBG}_{\text{ox}} + \text{NADH}$	$k_{\text{red}} 2.0 \times 10^6 \text{ M}^{-1} \text{ s}^{-1}$	$k_{\text{ox}} 2.0 \times 10^6 \text{ M}^{-1} \text{ s}^{-1}$
Mediator dependent		
$\text{MV}^{2+} + \text{FdsBG}_{\text{ox}} \rightleftharpoons \text{MV}^{2+} + \text{FdsBG}_{\text{int}}$	$k_3 3.5 \times 10^7 \text{ M}^{-1} \text{ s}^{-1}$	$k_4 3.5 \times 10^4 \text{ M}^{-1} \text{ s}^{-1}$
$\text{MV}^{2+} + \text{FdsBG}_{\text{int}} \rightleftharpoons \text{MV}^{2+} + \text{FdsBG}_{\text{red}}$	$k_3^a 3.5 \times 10^7 \text{ M}^{-1} \text{ s}^{-1}$	$k_4^b 3.5 \times 10^4 \text{ M}^{-1} \text{ s}^{-1}$
$\text{MB}^+ + \text{FdsBG}_{\text{red}} \rightleftharpoons \text{MBH} + \text{FdsBG}_{\text{ox}}$	$k_5 1.6 \times 10^7 \text{ M}^{-1} \text{ s}^{-1}$	$k_6 1.6 \times 10^3 \text{ M}^{-1} \text{ s}^{-1}$

<sup>a</sup>  $k_3$  assumed to be equal for reduction of  $\text{FdsBG}_{\text{ox}}$  and  $\text{FdsBG}_{\text{int}}$ . <sup>b</sup>  $k_4$  assumed to be equal for oxidation of  $\text{FdsBG}_{\text{int}}$  and  $\text{FdsBG}_{\text{red}}$ .



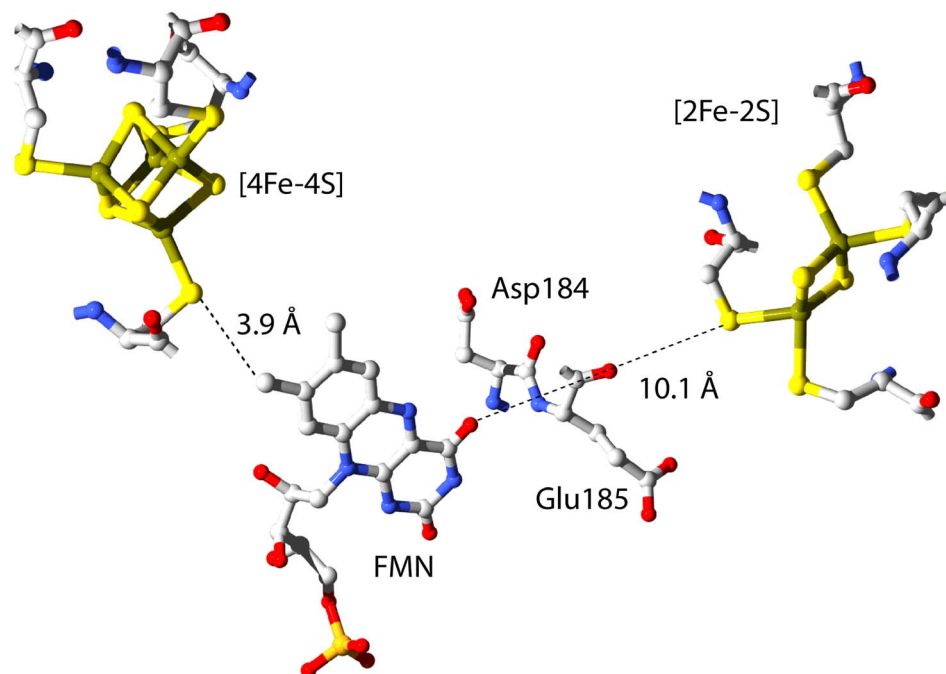


Fig. 2 The relative positions of the three redox active cofactors in FdsBG. Coordinates were taken from the published X-ray crystal structure (PDB 6VW7).<sup>24</sup>

of the two Fe–S clusters. The transition from fully oxidised to fully (four-electron) reduced FdsBG theoretically involves five different UV-vis spectra and four redox potentials. A simultaneous global fit of so many parameters is not practical. The redox potentials of the three cofactors are sufficiently well separated that the entire set of potential-dependent spectra could be broken into three sections (here designated ‘low’, ‘mid’ and ‘high’ potential) and analysed individually as one- or two-electron steps. All potential-dependent spectra are shown in the ESI (Fig. S2A–C)<sup>†</sup> and the three partially overlapping sections are illustrated in a single wavelength plot (at 460 nm) as a function of potential and pH (Fig. S2D)<sup>†</sup>. This plot shows the stepwise decrease in absorbance at 460 nm upon reduction which is then reversed on oxidation. Data at pH 7 are shown in Fig. 3A–F, while remaining raw data and spectral analyses are in the ESI (Fig. S3 and S4).<sup>†</sup>

The  $[2\text{Fe}-2\text{S}]^{2+}$  cluster in the FdsG subunit is reduced first in a single electron reaction ( $[2\text{Fe}-2\text{S}]^{2+/+}$ ). However, as noted previously,<sup>24,27</sup> this region comprises two closely separated one-electron steps due to the  $[2\text{Fe}-2\text{S}]^{2+/+}$  clusters of FdsBG and its deflavo form (*i.e.* lacking FMN), which comprises 50% of the total protein sample. The potential-dependent spectra were separated into two regions and modelled as independent one-electron redox reactions (eqn (1)) with the truncated potential ranges (yellow and blue dots in Fig. 3B) avoiding spectral overlap from the two chromophores as much as possible. The spectra in this region (Fig. 3A) are dominated by transitions from the underlying oxidised FMN cofactor, so changes due to  $[2\text{Fe}-2\text{S}]^{2+}$  cluster reduction are more clearly appreciated by viewing their difference spectra (Fig. 3A, inset) which show the difference maxima (at 571, 479 and 364 nm) characteristic of the

$[2\text{Fe}-2\text{S}]^{2+}$  cluster, given that the spectrum of reduced  $[2\text{Fe}-2\text{S}]^{+}$  is featureless.<sup>50–52</sup> The absence of the FMN cofactor in deflavo-FdsBG evidently influences the redox potential of the  $[2\text{Fe}-2\text{S}]$  cluster but an unambiguous assignment of the two  $[2\text{Fe}-2\text{S}]^{2+/+}$  couples to holo-FdsBG or deflavo-FdsBG is difficult. It is known from X-ray crystallography<sup>24</sup> that there is a significant conformational change going from holo-FdsBG to deflavo-FdsBG especially involving residues Asp184 and Glu185 (Fig. 2). No significant pH dependence of these potentials was found (Table 1).

FMN reduction was modelled as consecutive one-electron reactions (eqn (2)) at each pH value for the two half-potentials  $\text{FMN}/\text{FMNH}^{\cdot}$  and  $\text{FMNH}^{\cdot}/\text{FMNH}^{-}$ . However, the two couples are in proximity so the semiquinone  $\text{FMNH}^{\cdot}$  is unstable with respect to disproportionation to the fully oxidised (FMN) and reduced ( $\text{FMNH}^{-}$ ) forms. The calculated spectrum of the flavin semiquinone contributes minimally due to its negligible accumulation at all potentials. Previously reported time-resolved stopped flow measurements allowed the UV-vis and EPR spectra of the metastable transient  $\text{FMNH}^{\cdot}$  form to be captured<sup>24</sup> which decayed rapidly (within seconds). Under the equilibrium conditions employed here there was no possibility of observing the semiquinone radical. Across the potential range  $-250$  to  $-400$  mV the prominent maxima from the FMN chromophore essentially vanish (Fig. 3C). The difference spectrum over this region between the fully oxidised and reduced flavin (Fig. 3C, inset) highlights the FMN chromophore with its characteristic maxima at 452 and 375 nm typical of oxidised flavin cofactors.<sup>53</sup> One notable feature is that the change in molar absorptivity (Fig. 3C, inset) is only  $\sim 5000 \text{ M}^{-1} \text{ cm}^{-1}$ , which is approximately half of the expected value for reduction



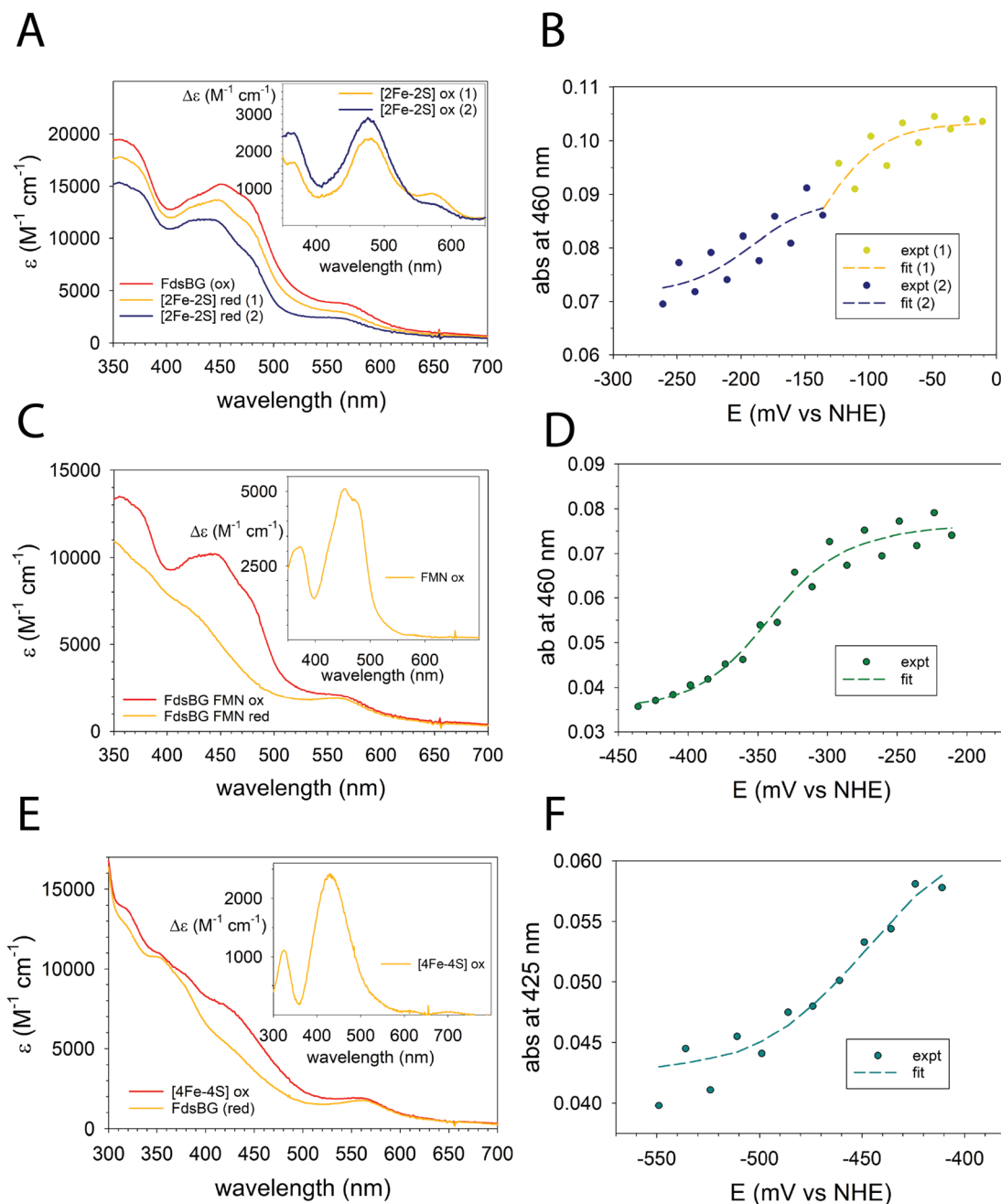


**Fig. 3** ReactLab redox spectral analysis for FdsBG (100  $\mu\text{M}$ , pH 7) showing the (A) calculated spectra from the high potential region  $-0.26 < E < 0$  V vs. NHE (red 1 and red 2 correspond to the one electron reduced flavo- and deflavo-FdsBG proteins); (B) calculated (broken lines) and experimental absorbances at 460 nm as a function of potential ( $E_1 -0.11$  V,  $E_2 -0.19$  V); (C) calculated spectra from the mid potential region  $-0.45 < E < -0.21$  V; (D) calculated (broken line) and experimental absorbances at 460 nm as a function of potential ( $E_1 -0.25$ ,  $E_2 -0.34$  V); (E) calculated spectra from the low potential region  $-0.55 < E < -0.41$  V; (F) calculated (broken line) and experimental absorbances at 425 nm as a function of potential ( $E_1 -0.45$  V). The mediators present (all 80  $\mu\text{M}$ ) are  $[\text{Fe}(\text{trans-diammac})]^{3+}$ ,  $[\text{Co}(\text{AMMEN}_4\text{S}_2\text{sar})]^{3+}$ ,  $[\text{Co}(\text{AMMEN}_5\text{Ssar})]^{3+}$ ,  $[\text{Co}(\text{sep})]^{3+}$ ,  $[\text{Co}(\text{AMMEsar})]^{3+}$ ,  $[\text{Co}(\text{ClMeClAbsar})]^{3+}$  and  $[\text{Co}(\text{cis-diammac})]^{3+}$ . See ESI† for their chemical structures. The insets to panels (A, C and E) are the difference spectra calculated from the spectral data in each main panel.

of a flavin chromophore. As mentioned above, the protein mixture comprises *ca.* 50% deflavo-FdsBG which accounts for the smaller than usual change in spectrum. As protonation accompanies reduction of FMN, the midpoint potentials shift negatively as the pH rises, but the observed shifts (Table 1) are small and much less than expected for a  $2e^-/2H^+$  reaction

( $-59$  mV  $\text{pH}^{-1}$ ); the data are more consistent with an overall  $2e^-/H^+$  reaction ( $-29.5$  mV  $\text{pH}^{-1}$ ). The  $\text{pK}_a$  of  $\text{FMNH}^+$  semi-quinones in flavoproteins are typically too high to be measured potentiometrically<sup>54</sup> so proton transfer accompanies the first reduction while the second electron transfer generates the monoanion.



For the  $[4\text{Fe-4S}]^{2+}$  cluster, a modest decrease in absorbance in the range 400–500 nm was apparent (Fig. 3E) upon electrochemical reduction, which is characteristic of a  $[4\text{Fe-4S}]^{2+}$  cluster.<sup>55–57</sup> The difference spectrum (Fig. 3E, inset) accentuates this feature. Of the three chromophores present, the overall absorbance changes for the  $[4\text{Fe-4S}]^{2+}$  cluster were the smallest. A more challenging issue was that data collected at large negative potentials at pH 6 were compromised by hydrogen evolution (bubbles) in the spectral beam. For the remaining data, no significant change in the  $[4\text{Fe-4S}]^{2+/+}$  redox potential was observed between pH 7 and pH 8 (Table 1) including the published data at pH 7.5.<sup>27</sup> Only a single potential-dependent spectral change was apparent so the  $[4\text{Fe-4S}]^{2+/+}$  potentials of the FdsBG holoprotein and its de flavo form must be very similar.

### Cyclic voltammetry

Electrochemical methods were applied in characterising the catalytic activity of the subcomplex FdsBG toward  $\text{NAD}^+$  reduction and NADH oxidation. For all experiments the concentration of FMN-containing FdsBG was used as the de flavo form cannot react with either  $\text{NAD}^+$  or NADH.

**FdsBG-catalysed  $\text{NAD}^+$  reduction.** FdsBG-catalysed  $\text{NAD}^+$  reduction was investigated using electrochemically reduced methyl viologen ( $\text{MV}^{2+}$ ) as the electron donor. The pH dependence of FdsDABG formate dehydrogenases has been well studied with optimal activity for formate oxidation typically around pH 7.5.<sup>19,42,58</sup> Additionally,  $\text{MV}^{2+/+}$  has been explored as a mediator supporting  $\text{CO}_2$  reductase activity for other formate dehydrogenase enzymes.<sup>59,60</sup> In the present study, the substrate being reduced is  $\text{NAD}^+$  (rather than  $\text{CO}_2$ ) and the FMN cofactor in the FdsB subunit is the active site.

The cyclic voltammetry response of  $\text{MV}^{2+}$  with FdsBG gave the expected single electron, quasi-reversible  $\text{MV}^{2+/+}$  redox response ( $E' = -0.43$  V vs. NHE) with a peak-to-peak separation of 70 mV and anodic/cathodic peak current ratio of unity (Fig. 4A, black curve). Upon the addition of  $\text{NAD}^+$ , the

symmetrical  $\text{MV}^{2+/+}$  response changed initially to an asymmetric waveform then eventually to a sigmoidal shape accompanied by an approximately five-fold increase in cathodic current (Fig. 4A). This change in shape is indicative of an electrocatalytic ( $\text{EC}_{\text{cat}}$ ) mechanism. At high concentrations of  $\text{NAD}^+$  ( $>4$  mM) a steady state is reached where the rate of FdsBG reduction by  $\text{MV}^{2+}$  is equal to the rate of  $\text{NAD}^+$  turnover by reduced FdsBG. The limiting catalytic peak current ( $i_{\text{lim}}$ ) at  $-0.55$  V vs. NHE as a function of  $\text{NAD}^+$  concentration was modelled with eqn (4) and an apparent Michaelis constant was calculated ( $K_{\text{M,NAD}^+} = 1.2(1)$  mM, Fig. 4B). Biochemical analysis of the highly homologous FdsBG (from *R. capsulatus*) found a similar value for  $\text{NAD}^+$  reduction ( $K_{\text{M,NAD}^+} 1.1$  mM).<sup>25</sup> As a control, in the absence of FdsBG, no enhancement of  $\text{MV}^{2+}$  cathodic current is seen upon addition of  $\text{NAD}^+$  (Fig. S5†).

The less negative redox potential mediator safranin T (Fig. S1,†  $E' = -0.29$  V vs. NHE, pH 7) gave no change in current as a function of  $\text{NAD}^+$  concentration (data not shown). Given that the redox potential of the  $\text{NAD}^+/\text{NADH}$  couple ( $-0.32$  V, pH 7)<sup>61</sup> is more negative than safranin T this was not unexpected. However, simple thermodynamic arguments alone do not predict the rates of outer sphere electron transfer between mediator and FdsBG. The mediators  $[\text{Co}(\text{ClMeClAbsar})]^{3+/2+}$  ( $-0.45$  V vs. NHE),  $[\text{Co}(\text{cis-diammac})]^{3+/2+}$  ( $-0.50$  V, Fig. S1†) were also tested as mediators but neither could support FdsBG-catalysed  $\text{NAD}^+$  reduction. Clearly this is not a thermodynamic constraint as  $[\text{Co}(\text{ClMeClAbsar})]^{2+}$  and  $[\text{Co}(\text{cis-diammac})]^{2+}$  are similarly strong reductants as  $\text{MV}^{2+}$  ( $-0.43$  V). Furthermore, these complexes in their  $\text{Co}^{\text{II}}$  state can reduce FdsBG as shown by UV-vis spectroelectrochemistry (Fig. 3 and ESI Fig. S2–S4†). In this case, the absence of a catalytic current is due to kinetic limitations where  $\text{Co}^{\text{II}}$ -mediated reduction of FdsBG is too slow to sustain catalysis. The organic mediator  $\text{MV}^{2+/+}$  is flat and like  $\text{NAD}^+/\text{NADH}$  may enter the binding pocket adjacent to the FMN cofactor for rapid electron transfer while the larger coordination complexes are hindered, and electron transfer is slowed significantly.

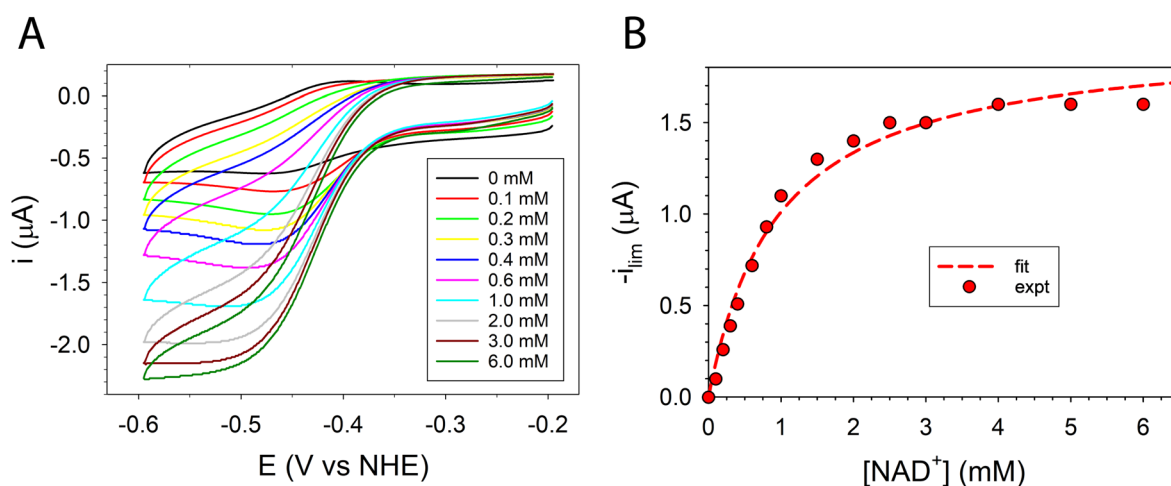


Fig. 4 (A) CVs of methyl viologen ( $60 \mu\text{M}$ ) in buffer ( $50 \text{ mM}$  phosphate, pH 7.5) containing FdsBG ( $0.34 \mu\text{M}$ ) at increasing concentrations of  $\text{NAD}^+$  ( $0$ – $6 \text{ mM}$ ). (B) Plot of baseline subtracted electrocatalytic limiting cathodic current ( $\mu\text{A}$  at  $-0.55$  V vs. NHE) against  $\text{NAD}^+$  concentration and fit to eqn (4) ( $K_{\text{M,NAD}^+} = 1.2(1)$  mM).





**FdsBG-catalysed NADH oxidation.** As mentioned, most metal-dependent formate dehydrogenases are bidirectional and can also catalyse  $\text{CO}_2$  reduction to formate. As the site of hydride exchange with  $\text{NADH}/\text{NAD}^+$  is still the FMN cofactor, this implies that the FdsBG subcomplex should also be bidirectional and biochemical studies on this enzyme<sup>20,24</sup> and the highly homologous *R. capsulatus* FdsBG<sup>25</sup> have supported this. Here, we investigated FdsBG  $\text{NADH}:\text{O}_2$  oxidoreductase (diaphorase) activity electrochemically but with mediators that have redox potentials more positive than the  $\text{NAD}^+/\text{NADH}$  potential to bias the chemistry in favour of NADH oxidation. As above, control experiments were first explored to ensure that selected mediators did not oxidise NADH without FdsBG present. A range of common organic mediators (Fig. S1†) were tested including methylene blue ( $\text{MB}^+$ ) and phenazine methosulfate (PMS). In the absence of FdsBG, the reversible 2-electron response of PMS (Fig. S6†) showed an enhanced anodic current upon addition of NADH. This eliminated PMS as a practical mediator of FdsBG-catalysed NADH oxidation due to its indiscriminate oxidation activity.

Methylene blue was found to be the most suitable electron acceptor for FdsBG-catalysed NADH oxidation. Voltammetry of  $\text{MB}^+$  alone resulted in the expected quasi-reversible two-electron redox response ( $E' = +0.010$  V vs. NHE, pH 7) with a peak-to-peak separation of 70 mV (Fig. S7†). The addition of NADH (in excess) resulted in no significant increase in current although the waveform became less peak-shaped (flattened). Thermodynamically, NADH ( $E' -0.33$  V, pH 7) is capable of reducing  $\text{MB}^+$  (ref. 62 and 63) and bulk reduction of  $\text{MB}^+$  to its colourless leuco form ( $\text{MBH}$ ) was observed upon addition of excess NADH to the electrochemical cell. However, this reaction is slow on the voltammetric timescale as no enhancement in  $\text{MBH}$  oxidation current was found when NADH was added (Fig. S7†). Upon addition of FdsBG the anodic current increased as anticipated (Fig. S7†).

In the presence of FdsBG, the CV waveform of  $\text{MB}^+$  as a function of NADH concentration changed from symmetrical

to the typical asymmetric catalytic shape paired with a significant increase in anodic current (Fig. 5A). At approximately 400  $\mu\text{M}$  NADH, the catalytic anodic current reached saturation as expected for an enzyme-catalysed reaction and the cathodic peak of the wave vanished. The limiting catalytic peak current ( $i_{\text{lim}}$ ), corrected for the response of the mediator in the absence of NADH, was measured at +0.15 V vs. NHE as a function of NADH concentration (Fig. 5B), giving  $K_{\text{M,NADH}} = 1.7(1) \times 10^2$   $\mu\text{M}$ , (pH 7.5). Comparable biochemical data from the holoenzyme FdsDABG and the FdsBG subcomplex (*C. necator*) for NADH oxidation have been published with  $K_{\text{M,NADH}}$  (or  $K_{\text{d,NADH}}$ ) values of 46  $\mu\text{M}$ <sup>22</sup> and  $1.9 \times 10^2$   $\mu\text{M}$ ,<sup>24</sup> respectively. Data published for FdsBG (from *R. capsulatus*) reported a similar value of  $K_{\text{M,NADH}} 1.3 \times 10^2$   $\mu\text{M}$ .<sup>25</sup>

**pH dependence.** The pH dependence of MV-mediated FdsBG-catalysed  $\text{NAD}^+$  reduction was explored over the range pH 6–9. The catalytic current (at saturating  $\text{NAD}^+$  concentration) exhibited a bell-shaped profile (Fig. 6A) with a maximum at approximately pH 7.5. Application of eqn (5) yielded  $\text{pK}_a$  values of 8.4(1) and 6.3(1) (Fig. 6A). The pH-dependence of MB-mediated FdsBG-catalysed NADH oxidation (Fig. 6B) showed remarkably similar behaviour, with protonation constants (7.9(2) and 6.5(2)) that are not significantly different from the  $\text{NAD}^+$  reduction profile. All raw CV data are available in the ESI (Fig. S8).† These values match previously reported pH profiles for FdsDABG-catalysed formate oxidation and  $\text{CO}_2$  reduction.<sup>19,22,42,58</sup>

The similarity of the profiles in Fig. 6A and B and the same  $\text{pK}_a$  values found in the FdsDABG holoenzyme imply that acid-base reactions at the  $\text{NAD}^+/\text{NADH}$  binding FMN site, common to both enzymes, underpin the pH dependence of both FdsBG and FdsDABG catalysis. As shown by the spectroelectrochemistry results (Table 1) the redox potentials of the  $[\text{4Fe-4S}]$  cluster and  $[\text{2Fe-2S}]$  cluster are almost pH-independent while the FMN potential shifts slightly more negative at higher pH. The redox potential of  $\text{MV}^{2+/+}$  is pH independent, so the electrochemical driving force of the reductant does not

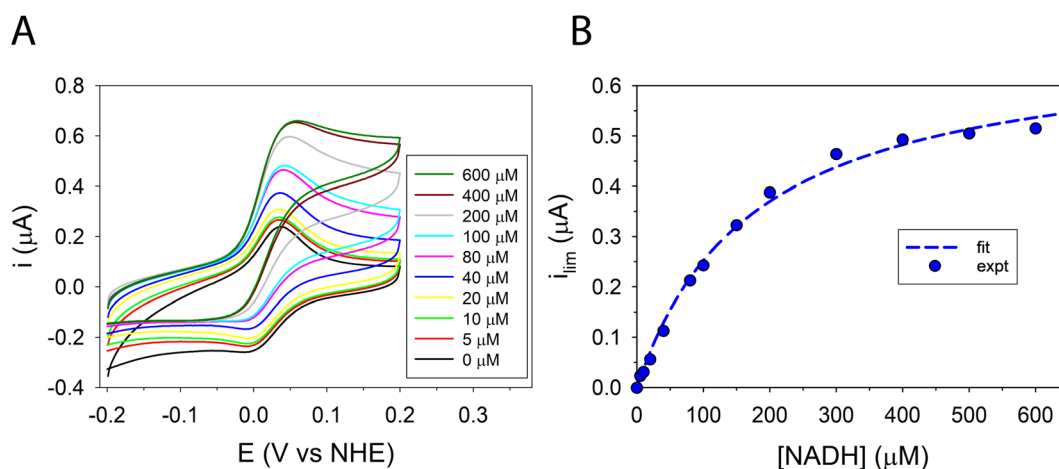


Fig. 5 (A) Selected CVs of methylene blue (20  $\mu\text{M}$ ) (50 mM phosphate buffer, pH 7.5) containing FdsBG (0.34  $\mu\text{M}$ ) at increasing concentrations of NADH (0–600  $\mu\text{M}$ ). (B) Plot of baseline subtracted electrocatalytic limiting cathodic current ( $\mu\text{A}$  at +0.15 V vs. NHE) against NADH concentration and fit to eqn (4) ( $K_{\text{M,NADH}} = 1.7(1) \times 10^2$   $\mu\text{M}$ ).

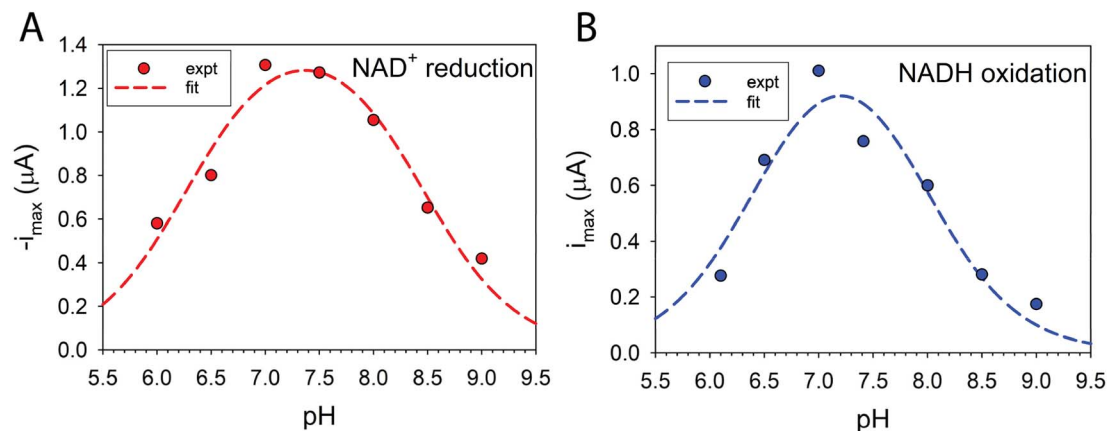


Fig. 6 pH dependence of FdsBG (0.34 μM) catalysed (A) NAD<sup>+</sup> (5 mM) reduction mediated by methyl viologen (60 μM) the broken curve is obtained from a fit to the experimental data using eqn (5) ( $pK_{a1} = 8.4(1)$ ,  $pK_{a2} = 6.3(1)$ ) and (B) NADH (500 μM) oxidation mediated by methylene blue (60 μM) the broken curve is obtained from a fit to the experimental data using eqn (5) ( $pK_{a1} = 7.9(2)$ ,  $pK_{a2} = 6.5(2)$ ). All CV data were collected at a scan rate of 5 mV s<sup>-1</sup>. The voltammograms are shown in the ESI (Fig. S8).†

change with pH for the system in Fig. 6A. The redox properties of the two-electron oxidant/reductant MB<sup>+</sup>/MBH are pH-dependent but not straightforward;<sup>64</sup> in the range  $6 < \text{pH} < 9$  the dependence is  $-29 \text{ mV pH}^{-1}$  (ref. 65) which equates to a  $2e^-/1H^+$  reaction in accord with the monocation MB<sup>+</sup> and neutral MBH forms being the redox active species.

The changes in cofactor and mediator redox potentials with pH are small and do not correlate with the data in Fig. 6A and B. The substrate NAD<sup>+</sup>/NADH redox potential ( $E' - 0.32 \text{ V vs. NHE}$  at pH 7) is pH-dependent with a shift of  $-29 \text{ mV pH}^{-1}$  unit.<sup>54</sup> At high pH, reduction of NAD<sup>+</sup> becomes thermodynamically and kinetically less favoured which may contribute to the drop in current on the basic limb of the profile but this does not explain the same trend apparent in the NADH oxidation profile as the MB<sup>+</sup>/MBH redox potential is always much more positive than the FMN/FMNH<sup>-</sup> (or NAD<sup>+</sup>/NADH) potential. Regarding the acidic limb of Fig. 6A, the X-ray crystal structure of FdsBG in complex with NADH (and in its absence) highlight several potential bases that may be involved in this modulation of activity. Two residues of interest are Asp184 and Glu185 (Fig. 2) which are close to the FMN group and form H-bonds (in their deprotonated forms) with the nicotinamide and/or FMN cofactor and protonation of these may disrupt the active site and weaken substrate binding. A more definitive explanation of the basic limbs of Fig. 6A and B remains the subject of further work.

**Electrochemical simulations.** Electrochemical simulations have been widely employed to understand biochemical kinetic and mechanistic properties of a redox active catalytic system.<sup>43,66–69</sup> The objective is to model all experimental CV data based on a given mechanism that involve homogeneous chemical reactions and both homogeneous and heterogeneous electron transfer steps. The correct rate and equilibrium constants associated with these steps, the mediator redox potentials and heterogeneous electron transfer kinetics will reproduce all CV data over a range of substrate concentrations and sweep rates. The models used to simulate MV-mediated FdsBG-catalysed NAD<sup>+</sup> reduction (Scheme 1A) and MB-

mediated FdsBG-catalysed NADH oxidation (Scheme 1B) define all kinetic parameters.

Although electrochemical analysis of electrode-confined (adsorbed) enzymes can also provide useful kinetic information,<sup>42,66–69</sup> an advantage of the present approach with all species in solution is that accurate enzyme concentrations are known, although consumption of enzyme can be significantly greater than experiments using electrode-confined enzyme. For FdsBG electrocatalysis experiments, the simulations were performed at multiple scan rates (2, 5, 10 and 20 mV s<sup>-1</sup>) and substrate concentrations (NAD<sup>+</sup>: 0–6 mM, NADH: 0–600 μM) guided by the data in Fig. 4 and 5. The rate constants defined in Scheme 1 and assembled in Table 2 reproduced the experimental voltammetry profiles across a range of scan rates, and substrate concentrations (Fig. 7 and 8).

Experimental and simulated CV data of MV<sup>2+</sup> (60 μM), FdsBG (0.34 μM) and NAD<sup>+</sup> (200 μM to 6 mM) at different scan rates are shown in Fig. 7. The theoretical aspects underpinning the changes in waveform in an enzyme-catalysed electrochemical system as a function of substrate concentration and scan rate are well described elsewhere<sup>70</sup> and also applied to synthetic (non-enzymatic) electrocatalysis where they are conveniently graphically represented by so-called kinetic zone diagrams.<sup>44,71,72</sup> In this case, competition between the enzyme-substrate reaction (a function of substrate concentration) and the enzyme-mediator reaction is the major cause of the changes in waveform here. Variations in scan rate can also affect the CV profile but in the systems studied here the scan rates were deliberately confined to a narrow range to avoid excessive charging currents relative to the faradaic currents at micromolar concentrations. All CVs fall into the so-called 'pure kinetic zone' with subtle changes in wave symmetry and shape attributable to substrate concentrations.

At low NAD<sup>+</sup> concentrations (200–600 μM), asymmetric peak-shaped curves are found where NAD<sup>+</sup> mass transport limits the cathodic current. As the NAD<sup>+</sup> concentration reaches saturating levels (~6 mM) sigmoidal waveforms emerge characteristic of an electrochemical steady state. The CVs under these



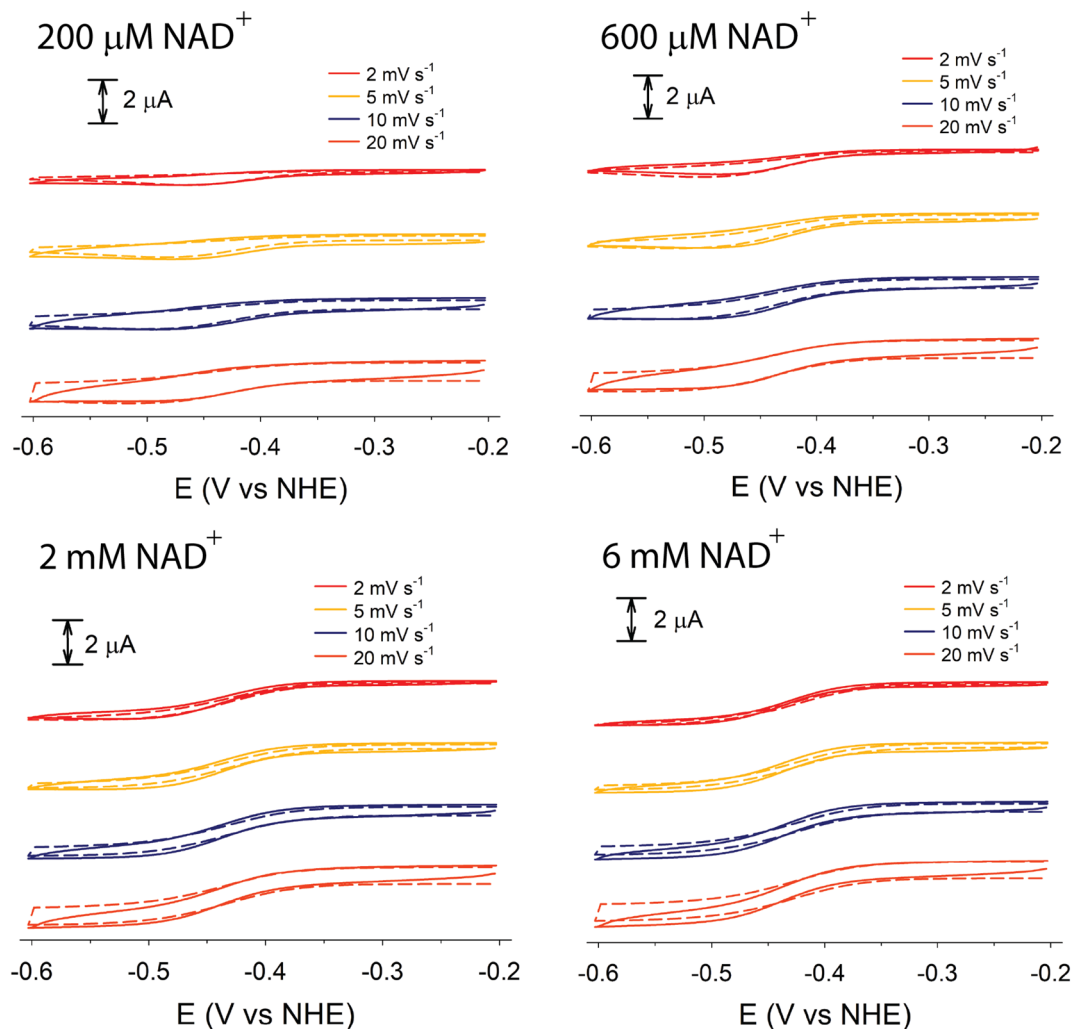


Fig. 7 Experimental (solid lines) and simulated (broken lines) cyclic voltammograms of methyl viologen (60  $\mu\text{M}$ ) mediated FdsBG (0.34  $\mu\text{M}$ ) catalysed  $\text{NAD}^+$  reduction (concentrations shown) at different scan rates (50 mM phosphate buffer, pH 7.5).

conditions are essentially independent of scan rate as the rate of the  $\text{FdsBG}_{\text{red}}:\text{NAD}^+$  reaction is at its maximum (limited by the turnover number). At faster scan rates (20  $\text{mV s}^{-1}$ ) and low  $\text{NAD}^+$  concentrations (200  $\mu\text{M}$ ), production of  $\text{MV}^{+\bullet}$  at the electrode exceeds its rate of consumption by  $\text{NAD}^+$ -oxidised FdsBG and an anodic peak due to unreacted  $\text{MV}^{+\bullet}$  reappears.

The CV data of  $\text{MB}^+$  (20  $\mu\text{M}$ ) in the presence of FdsBG (0.34  $\mu\text{M}$ ) and NADH (40–600  $\mu\text{M}$ ) at different scan rates are also shown (Fig. 8). Again, at slower scan rates (2, 5  $\text{mV s}^{-1}$ ) and low NADH concentrations (<100  $\mu\text{M}$ ), an asymmetric waveform is observed indicative of substrate limited currents where NADH depletion from the reaction layer attenuates catalysis. At higher NADH concentrations, the observed and simulated waveforms are more symmetrical and sigmoidal in shape although NADH depletion is still apparent in all CVs in Fig. 8 from the peak-shaped anodic profiles which is indicative of slower substrate turnover.

The CV waveforms are also sensitive to the electron transfer stoichiometry. The two-electron  $\text{MB}^+/\text{MBH}$  redox reaction shows noticeably steeper CV traces (Fig. 8) than the single-

electron  $\text{MV}^{2+/+}$  couple (Fig. 7) and this translates into similarly shaped catalytic profiles as expected.<sup>40</sup>

### Kinetic analysis

The overall kinetics of both the reduction of  $\text{NAD}^+$  and oxidation of NADH as catalysed by FdsBG conform to a two-substrate ping-pong mechanism as expected, with the enzyme alternating between reduced and oxidised forms. In principle, each catalytic cycle of the enzyme should consist of four steps: (i) substrate binding; (ii) turnover; (iii) product release and (iv) outer sphere electron transfer with the mediator to regenerate the active form of FdsBG (either reduced or oxidised). However, as will be shown, the unimolecular steps (ii) and (iii) are inseparable from (i) at practical experimental concentrations and scan rates and they therefore cannot be fitted independently within the same model. The scan rate and substrate concentration dependent data were modelled with a simpler scheme where substrate binding, turnover and product release are incorporated into a single bimolecular rate constant ( $k_{\text{red}}$  for  $\text{NAD}^+$  reduction or  $k_{\text{ox}}$  for the reverse NADH oxidation). Accurate rate constants describing enzyme



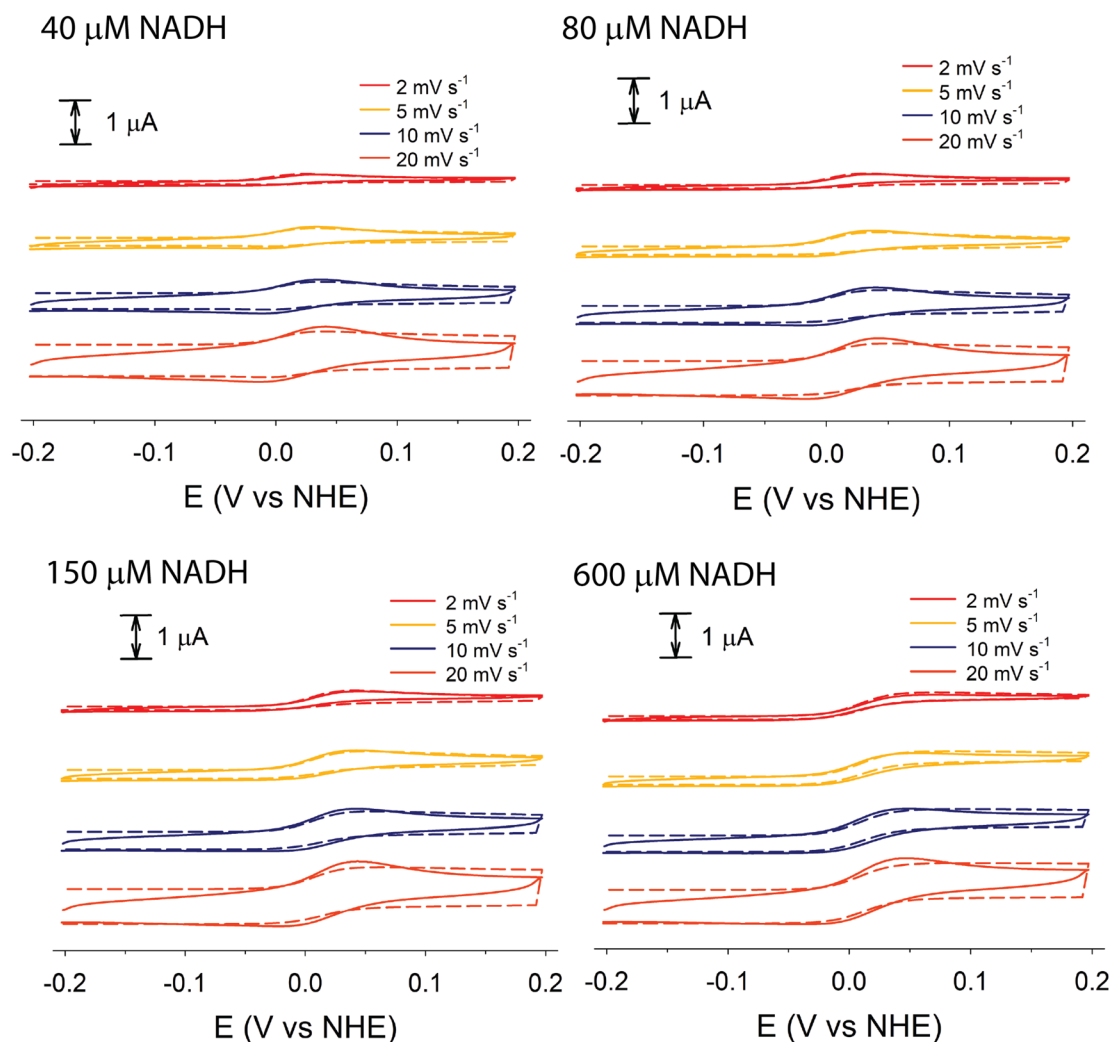
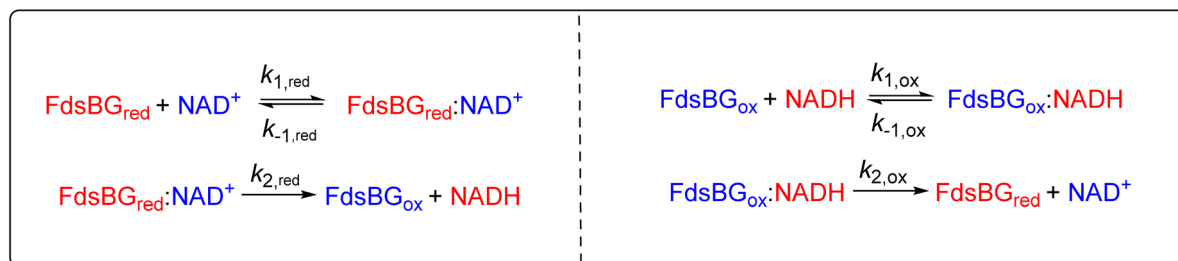


Fig. 8 Experimental (solid lines) simulated (broken lines) cyclic voltammograms of methylene blue (20  $\mu\text{M}$ ) mediated FdsBG (0.34  $\mu\text{M}$ ) catalysed NADH oxidation (concentrations shown) at different scan rates (50 mM phosphate buffer, pH 7.5).

reaction ( $k_{\text{ox}}$  and  $k_{\text{red}}$ , Table 2) emerge at low substrate concentrations (so-called pure kinetic conditions or zone K)<sup>71</sup> where substrate binding limits the catalytic current. The outer sphere electron transfer rate constants  $k_3/k_4$  (for MV-driven  $\text{NAD}^+$  reduction) and  $k_5/k_6$  (for MB-driven NADH oxidation) are accurately determined when the enzyme is saturated with substrate which give essentially sigmoidal profiles (within the zone KS).<sup>71</sup> It is relevant that reduction of FdsBG by  $\text{MV}^{2+}$  ( $k_3$ ) and oxidation of

FdsBG by  $\text{MB}^+$  ( $k_5$ ) are effectively irreversible reactions due to the large driving force involved, so the reverse outer sphere electron transfer rate constants ( $k_4$  and  $k_6$ ) are uncertain, and their values have no influence on the simulations. Also the rates of the consecutive one-electron  $\text{MV}^{2+}$  reductions of  $\text{FdsBG}_{\text{ox}}$  and  $\text{FdsBG}_{\text{int}}$  ( $k_3$ , Scheme 1) were assumed to be equal based on their very similar driving forces.



Scheme 2 Substrate binding and turnover steps for  $\text{NAD}^+$  reduction and NADH oxidation by FdsBG. The rate constants are elaborated in eqn (7)–(10) below.





The mediator-independent rate constants  $k_{\text{ox}}$  and  $k_{\text{red}}$  obtained from the simulations are the same at  $2.0 \times 10^6 \text{ M}^{-1} \text{ s}^{-1}$ , so the equilibrium constant for the reaction is unity. This is consistent with the midpoint potentials of the FMN cofactor ( $-0.34 \text{ V vs. NHE at pH 7.5}$ )<sup>27</sup> and the  $\text{NAD}^+/\text{NADH}$  couple ( $-0.33 \text{ V at pH 7.5}$ ) being the same within experimental error, meaning that the reaction is not biased in either direction.<sup>61</sup> However, the data in Fig. 4 and 5 reveal  $K_{\text{M},\text{NAD}^+}$  and  $K_{\text{M},\text{NADH}}$  values that differ by an order of magnitude. Following a typical Briggs–Haldane mechanism,<sup>73</sup> the rate constants  $k_{\text{red}}$  and  $k_{\text{ox}}$  are composites of substrate binding and turnover (Scheme 2) as expressed in eqn (7) and (8), respectively.

$$k_{\text{red}} = \frac{k_{1,\text{red}}k_{2,\text{red}}}{k_{-1,\text{red}} + k_{2,\text{red}}} = \frac{k_{2,\text{red}}}{K_{\text{M},\text{NAD}^+}} \quad (7)$$

$$k_{\text{ox}} = \frac{k_{1,\text{ox}}k_{2,\text{ox}}}{k_{-1,\text{ox}} + k_{2,\text{ox}}} = \frac{k_{2,\text{ox}}}{K_{\text{M},\text{NADH}}} \quad (8)$$

$$K_{\text{M},\text{NAD}^+} = \frac{k_{-1,\text{red}} + k_{2,\text{red}}}{k_{1,\text{red}}} = 1.2 \times 10^{-3} \text{ M} \quad (9)$$

$$K_{\text{M},\text{NADH}} = \frac{k_{-1,\text{ox}} + k_{2,\text{ox}}}{k_{1,\text{ox}}} = 1.7 \times 10^{-4} \text{ M} \quad (10)$$

Substituting the experimental values for  $K_{\text{M},\text{NAD}^+}$  (eqn (9)) and  $K_{\text{M},\text{NADH}}$  (eqn (10)) (see Fig. 4 and 5) and simulated  $k_{\text{ox}}/k_{\text{red}}$  values (Table 2) into eqn (7) and (8) generates turnover numbers of  $k_{2,\text{red}}$  ( $\text{NAD}^+$  reduction) =  $2.4 \times 10^3 \text{ s}^{-1}$  and  $k_{2,\text{ox}}$  ( $\text{NADH}$  oxidation) =  $3.4 \times 10^2 \text{ s}^{-1}$ . Pre-steady state kinetic investigations of FdsBG (*C. necator*)<sup>24</sup> revealed a limiting rate of  $\text{NADH}$  oxidation ( $6.8 \times 10^2 \text{ s}^{-1}$  at  $278 \text{ K}$ ) which greatly exceeded the corresponding rate of formate oxidation at the Mo active site by the FdsDABG holoenzyme.<sup>24</sup> Also of note are the large outer sphere electron transfer rate constants of FdsBG<sub>ox</sub> with  $\text{MV}^{+ \cdot}$  ( $k_3$ ) and FdsBG<sub>red</sub> with  $\text{MB}^+$  ( $k_5$ ) showing  $\text{MV}^{+ \cdot}$  and  $\text{MB}^+$  to be ideal artificial electron transfer partners. Electrochemical simulations with lower values for these rate constants could not produce the magnitudes of catalytic currents in Fig. 7 and 8 at saturating substrate concentrations regardless of substrate oxidation/reduction kinetics ( $k_{\text{ox}}$  and  $k_{\text{red}}$ ).

## Conclusions

This study has explored the redox properties and catalytic activity of the formate dehydrogenase subcomplex FdsBG including nicotinamide cofactor turnover, pH dependence, and optical spectroelectrochemistry, demonstrating how electrochemistry and simulations can be utilised to ascertain previously unknown kinetic properties of a  $\text{NADH}$  dehydrogenase enzyme. FdsBG provides an excellent enzymatic platform to explore the characteristics of both  $\text{NADH}$  oxidation and  $\text{NAD}^+$  reduction within the same system. The pH dependence of both the FdsBG redox potentials and  $\text{NAD}^+/\text{NADH}$  turnover have been obtained ( $6 < \text{pH} < 8$ ), augmenting previously reported electrochemical<sup>27</sup> and biochemical<sup>19,24</sup> data. To the best of our knowledge this is the first example of a full electrochemical

kinetic analysis of a reversible  $\text{NADH}$  dehydrogenase system. The parameters show that FdsBG is a highly active bidirectional catalyst of  $\text{NAD}^+/\text{NADH}$  turnover and also that  $\text{MV}^{+ \cdot}$  and  $\text{MB}^+$  are highly effective artificial electron partners to sustain catalysis and demonstrate the effectiveness of FdsBG in catalysing the electrochemical regeneration and interconversion of  $\text{NAD}^+$  and  $\text{NADH}$ . Opportunities to incorporate FdsBG as an electrochemically-driven generator of either  $\text{NADH}$  or  $\text{NAD}^+$  can now be considered coupled to other  $\text{NAD}^+/\text{NADH}$ -dependent enzymes.

## Data availability

Additional data supporting this article have been included as part of the ESI.†

## Author contributions

PDG: data curation, formal analysis, investigation, methodology, validation, writing – original draft, writing – review & editing. DN: resources – protein purification, writing – review & editing. SH: resources – protein purification, writing – review & editing. RH: funding acquisition, writing – review & editing. PVB: conceptualization, data curation, formal analysis, funding acquisition, methodology, project administration, resources, software, validation, visualization, writing – original draft, writing – review & editing.

## Conflicts of interest

There are no conflicts to declare.

## Acknowledgements

This work was supported by financial support of the Australian Research Council (Discovery Projects DP220103268 to PVB) and is gratefully acknowledged, as is support from the US Department of Energy (DE-SC0010666 to RH).

## Notes and references

- 1 X. Wang, T. Saba, H. H. P. Yiu, R. F. Howe, J. A. Anderson and J. Shi, *Chem*, 2017, **2**, 621–654.
- 2 S. Tian, G. Long, P. Zhou, F. Liu, X. Zhang, C. Ding and C. Li, *J. Am. Chem. Soc.*, 2024, **146**, 15730–15739.
- 3 E. Aamer, J. Thöming, M. Baune, N. Reimer, R. Dringen, M. Romero and I. Bösing, *Sci. Rep.*, 2022, **12**, 16380.
- 4 L. Tensi and A. Macchioni, *ACS Catal.*, 2020, **10**, 7945–7949.
- 5 C.-H. Wong and G. M. Whitesides, *J. Am. Chem. Soc.*, 2002, **124**, 4890–4899.
- 6 L. Lauterbach, O. Lenz and K. A. Vincent, *FEBS J.*, 2013, **280**, 3058–3068.
- 7 G. Xu, C. Zhu, A. Li, Y. Ni, R. Han, J. Zhou and Y. Ni, *ACS Sustainable Chem. Eng.*, 2019, **7**, 15706–15714.
- 8 Q. Jia, Y. C. Zheng, H. P. Li, X. L. Qian, Z. J. Zhang and J. H. Xu, *Appl. Environ. Microbiol.*, 2022, **88**, e0034122.



- 9 T. W. Johannes, R. D. Woodyer and H. Zhao, *Biotechnol. Bioeng.*, 2007, **96**, 18–26.
- 10 L. Zhang, E. King, W. B. Black, C. M. Heckmann, A. Wolder, Y. Cui, F. Nicklen, J. B. Siegel, R. Luo, C. E. Paul and H. Li, *Nat. Commun.*, 2022, **13**, 5021.
- 11 W. Ma, Q. Geng, C. Chen, Y. C. Zheng, H. L. Yu and J. H. Xu, *ChemBioChem*, 2023, **24**, e202300390.
- 12 A. Maier, T. Knaus, F. G. Mutti and D. Tischler, *ACS Catal.*, 2024, **14**, 2207–2215.
- 13 K. Seelbach, B. Riebel, W. Hummel, M.-R. Kula, V. I. Tishkov, A. M. Egorov, C. Wandrey and U. Kragl, *Tetrahedron Lett.*, 1996, **37**, 1377–1380.
- 14 J. Tian, D. G. Boggs, P. H. Donnan, G. T. Barroso, A. A. Garcia, D. P. Dowling, J. A. Buss and J. Bridwell-Rabb, *J. Biol. Chem.*, 2023, **299**, 105222.
- 15 S.-M. Jo, F. R. Wurm and K. Landfester, *Angew. Chem., Int. Ed.*, 2021, **60**, 7728–7734.
- 16 T. Knaus, W. Bohmer and F. G. Mutti, *Green Chem.*, 2017, **19**, 453–463.
- 17 S. C. Cosgrove, A. Brzezniak, S. P. France, J. I. Ramsden, J. Mangas-Sanchez, S. L. Montgomery, R. S. Heath and N. J. Turner, *Methods Enzymol.*, 2018, **608**, 131–149.
- 18 S. Hakopian, D. Niks and R. Hille, *J. Inorg. Biochem.*, 2022, **231**, 111788.
- 19 D. Niks, J. Duvvuru, M. Escalona and R. Hille, *J. Biol. Chem.*, 2016, **291**, 1162–1174.
- 20 R. Hille, T. Young, D. Niks, S. Hakopian, T. K. Tam, X. Yu, A. Mulchandani and G. M. Blaha, *Inorganics*, 2020, **8**, 41.
- 21 X. Yu, D. Niks, X. Ge, H. Liu, R. Hille and A. Mulchandani, *Biochemistry*, 2019, **58**, 1861–1868.
- 22 X. Yu, D. Niks, A. Mulchandani and R. Hille, *J. Biol. Chem.*, 2017, **292**, 16872–16879.
- 23 C. Radon, G. Mittelstadt, B. R. Duffus, J. Burger, T. Hartmann, T. Mielke, C. Teutloff, S. Leimkühler and P. Wendler, *Nat. Commun.*, 2020, **11**, 1912.
- 24 T. Young, D. Niks, S. Hakopian, T. K. Tam, X. Yu, R. Hille and G. M. Blaha, *J. Biol. Chem.*, 2020, **295**, 6570–6585.
- 25 T. Hartmann and S. Leimkühler, *FEBS J.*, 2013, **280**, 6083–6096.
- 26 D. Niks, S. Hakopian, A. Canchola, Y. H. Lin and R. Hille, *J. Am. Chem. Soc.*, 2024, **146**, 28601–28604.
- 27 J. R. Harmer, S. Hakopian, D. Niks, R. Hille and P. V. Bernhardt, *J. Am. Chem. Soc.*, 2023, **145**, 25850–25863.
- 28 B. R. Duffus, M. Gauglitz, C. Teutloff and S. Leimkühler, *J. Inorg. Biochem.*, 2024, **253**, 112487.
- 29 H. A. Reeve, L. Lauterbach, P. A. Ash, O. Lenz and K. A. Vincent, *Chem. Commun.*, 2012, **48**, 1589–1591.
- 30 H. A. Reeve, J. Nicholson, F. Altaf, T. H. Lonsdale, J. Preissler, L. Lauterbach, O. Lenz, S. Leimkühler, F. Hollmann, C. E. Paul and K. A. Vincent, *Chem. Commun.*, 2022, **58**, 10540–10543.
- 31 P. V. Bernhardt, P. Comba, T. W. Hambley and G. A. Lawrance, *Inorg. Chem.*, 1991, **30**, 942–946.
- 32 T. M. Donlevy, L. R. Gahan, T. W. Hambley and R. Stranger, *Inorg. Chem.*, 1992, **31**, 4376–4382.
- 33 J. I. Bruce, L. R. Gahan, T. W. Hambley and R. Stranger, *Inorg. Chem.*, 1993, **32**, 5997–6002.
- 34 I. Creaser, R. Geue, J. M. Harrowfield, A. Herlt, A. Sargeson, M. Snow and J. Springborg, *J. Am. Chem. Soc.*, 1982, **104**, 6016–6025.
- 35 R. Geue, T. Hambley, J. Harrowfield, A. Sargeson and M. Snow, *J. Am. Chem. Soc.*, 1984, **106**, 5478–5488.
- 36 P. V. Bernhardt, P. Comba and T. W. Hambley, *Inorg. Chem.*, 1993, **32**, 2804–2809.
- 37 P. V. Bernhardt, K. I. Chen and P. C. Sharpe, *J. Biol. Inorg. Chem.*, 2006, **11**, 930–936.
- 38 F. M. C. He and P. V. Bernhardt, *J. Biol. Inorg. Chem.*, 2017, **22**, 775–788.
- 39 M. Maeder and P. King, *ReactLab-Redox*, Jplus Consulting Pty Ltd, Perth, Western Australia, 2016.
- 40 A. J. Bard and L. R. Faulkner, *Electrochemical Methods: Fundamentals and Applications*, Wiley, 2001.
- 41 N. Anicet, C. Bourdillon, J. Moiroux and J.-M. Savéant, *J. Phys. Chem. B*, 1998, **102**, 9844–9849.
- 42 P. Kalimuthu, S. Hakopian, D. Niks, R. Hille and P. V. Bernhardt, *J. Phys. Chem. B*, 2023, **127**, 8382–8392.
- 43 P. Kalimuthu, D. Hege, A. Winiarska, Y. Gemmecker, M. Szaleniec, J. Heider and P. V. Bernhardt, *Chem.-Eur. J.*, 2023, **29**, e202203072.
- 44 J.-M. Savéant, *Chem. Rev.*, 2008, **108**, 2348–2378.
- 45 P. V. Bernhardt, *Aust. J. Chem.*, 2006, **59**, 233–256.
- 46 M. Rudolph, D. P. Reddy and S. W. Feldberg, *Anal. Chem.*, 1994, **66**, 589A–600A.
- 47 C. E. Banks and R. G. Compton, *Analyst*, 2005, **130**, 1232–1239.
- 48 M. E. Young, P. A. Carroad and R. L. Bell, *Biotechnol. Bioeng.*, 1980, **22**, 947–955.
- 49 J. Zapiter, J. R. Harmer, M. Struwe, A. Scheidig, B. Clement and P. V. Bernhardt, *Anal. Chem.*, 2022, **94**, 9208–9215.
- 50 S. G. Lloyd, R. Franco, J. J. G. Moura, I. Moura, G. C. Ferreira and B. H. Huynh, *J. Am. Chem. Soc.*, 1996, **118**, 9892–9900.
- 51 P. Yuvaniyama, J. N. Agar, V. L. Cash, M. K. Johnson and D. R. Dean, *Proc. Natl. Acad. Sci. U. S. A.*, 2000, **97**, 599–604.
- 52 H. Matsubara and K. Saeki, in *Adv. Inorg. Chem.*, ed. R. Cammack, Academic Press, 1992, vol. 38, pp. 223–280.
- 53 R. A. Copeland and T. G. Spiro, *J. Phys. Chem.*, 1986, **90**, 6648–6654.
- 54 S. G. Mayhew, G. P. Foust and V. Massey, *J. Biol. Chem.*, 1969, **244**, 803–810.
- 55 P. Kyritsis, O. M. Hatzfeld, T. A. Link and J. M. Moulis, *J. Biol. Chem.*, 1998, **273**, 15404–15411.
- 56 A. Jain, A. Singh, N. Maio and T. A. Rouault, *Hum. Mol. Genet.*, 2020, **29**, 3165–3182.
- 57 S. A. Child, J. M. Bradley, T. L. Pukala, D. A. Svistunenko, N. E. Le Brun and S. G. Bell, *Chem. Sci.*, 2018, **9**, 7948–7957.
- 58 J. Friedebold and B. Bowien, *J. Bacteriol.*, 1993, **175**, 4719–4728.
- 59 B. S. Jayathilake, S. Bhattacharya, N. Vaidehi and S. R. Narayanan, *Acc. Chem. Res.*, 2019, **52**, 676–685.
- 60 A. Miyaji and Y. Amao, *Phys. Chem. Chem. Phys.*, 2020, **22**, 18595–18605.
- 61 F. L. Rodkey, *J. Biol. Chem.*, 1955, **213**, 777–786.
- 62 J. F. J. Engbersen, A. Koudijs and H. C. van der Plas, *Recl. Trav. Chim. Pays-Bas*, 2010, **104**, 131–138.



- 63 P. Sevcik and H. B. Dunford, *J. Phys. Chem.*, 2002, **95**, 2411–2415.
- 64 W. M. Clark, *Oxidation Reduction Potentials of Organic Systems*, The Williams and Wilkins Company, Baltimore, USA, 1960.
- 65 H. Ju, J. Zhou, C. Cai and H. Chen, *Electroanalysis*, 1995, **7**, 1165–1170.
- 66 P. Kalimuthu, K. Fischer-Schrader, G. Schwarz and P. V. Bernhardt, *J. Phys. Chem. B*, 2013, **117**, 7569–7577.
- 67 P. Kalimuthu, J. R. Harmer, M. Baldauf, A. H. Hassan, T. Kruse and P. V. Bernhardt, *Biochim. Biophys. Acta, Bioenerg.*, 2022, **1863**, 148523.
- 68 P. Kalimuthu, M. D. Heath, J. M. Santini, U. Kappler and P. V. Bernhardt, *Biochim. Biophys. Acta*, 2014, **1837**, 112–120.
- 69 P. Kalimuthu, U. Kappler and P. V. Bernhardt, *J. Phys. Chem. B*, 2014, **118**, 7091–7099.
- 70 C. Bourdillon, C. Demaille, J. Moiroux and J. M. Savéant, *J. Am. Chem. Soc.*, 1993, **115**, 1–10.
- 71 E. S. Rountree, B. D. McCarthy, T. T. Eisenhart and J. L. Dempsey, *Inorg. Chem.*, 2014, **53**, 9983–10002.
- 72 J. M. Savéant and K. B. Su, *J. Electroanal. Chem. Interfacial Electrochem.*, 1984, **171**, 341–349.
- 73 A. Fersht, *Enzyme Structure and Mechanism*, W. H. Freeman and Company, San Francisco (USA) and Reading (UK), 1977.

